Performance Evaluation of the Time-of-Flight Biograph Vision.X: A Fast Coincidence Time Resolution PET/CT Scanner

Habib Zaidi, *Fellow, IEEE*, Yazdan Salimi, Mehdi Amini, Gregory Mathoux, Ismini Mainta, and Valentina Garibotto

Abstract*—This work evaluated the performance characteristics of the Biograph Vision.X PET/CT system according to the National Electrical Manufacturers Association (NEMA) NU 2-2018 standards. This novel system is based on the Biograph Vision 600 with an axial field-of-view (FOV) of 26.1 cm, consisting of 8 rings of 38 detector blocks using the same detector modules combining 5 × 5 array of 3.2 × 3.2 × 20 mm lutetium-oxyorthosilicate crystals with 16 × 16 mm array of silicon photomultiplier-based photodetectors. The Biograph Vision.X scanner is a newly released time-of-flight (TOF) whole-body hybrid PET/CT imaging system featuring exclusive proprietary high-performance detector electronic assembly (DEA) technology with optimized digital electronics and digital processing along the entire imaging chain to achieve fast coincidence time resolution PET. In addition, examples of 3-D Hoffman phantom and clinical ^{18}F-FDG brain and whole-body studies were compared with scans performed sequentially after the Biograph Vision 600 PET/CT scanner. The Biograph Vision.X had a radial, tangential and axial spatial resolution in terms of full-width at half-maximum of 3.4, 3.5, and 3.5 mm, respectively, at a 1 cm offset from the center of the FOV. The sensitivity was 19.2 cps/kBq at the center and 10 cm off-center, while the peak noise-equivalent count-rate (NECR) was 291 kcps at 27.2 kBq/mL. The TOF resolution varied from 178.7 to 182.0 ps as the count rate increased up to the peak NECR. Generally, the image contrast observed on the NEMA image quality phantom ranged from 74.1% to 91.8%. The Biograph Vision.X is a competitive newly introduced device outperforming its predecessor, the Biograph Vision 600, by reaching the fastest TOF performance in the industry, thus achieving ∼7.5 TOF gain improvement compared to 6.2 on the Vision 600.

Received 6 May 2025; revised 27 October 2025 and 28 November 2025; accepted 2 December 2025. This work was supported in part by the Swiss National Science Foundation under Grant SNSF 320030-231742, and in part by the Private Foundation of Geneva University Hospitals under Grant RC-06-01. *(Corresponding author: Habib Zaidi.)*

This work involved human subjects or animals in its research. Approval of all ethical and experimental procedures and protocols was granted by the Ethics Committee of the Geneva Canton under Application No. 2024-02232.

Habib Zaidi is with the Division of Nuclear Medicine and Molecular Imaging, Geneva University Hospital, 1205 Geneva, Switzerland, also with the Department of Nuclear Medicine and Molecular Imaging, University of Groningen, 9712 CP, Groningen, The Netherlands, also with the Department of Nuclear Medicine, University of Southern Denmark, 5230 Odense, Denmark, and also with the University Research and Innovation Center, Óbuda University, 1034 Budapest, Hungary (e-mail: habib.zaidi@hug.ch).

Yazdan Salimi, Mehdi Amini, Gregory Mathoux, Ismini Mainta, and Valentina Garibotto are with the Division of Nuclear Medicine and Molecular Imaging, Geneva University Hospital, 1205 Geneva, Switzerland

This article has supplementary material provided by the authors and color versions of one or more figures available at https://doi.org/10.1109/TRPMS.2025.3640401.

Digital Object Identifier 10.1109/TRPMS.2025.3640401

***Index Terms*—Image quality, National Electrical Manufacturers Association (NEMA), performance evaluation, PET/CT, time-of-flight (TOF).**

I. Introduction

PET IS a well-established molecular imaging modality used worldwide to study the molecular pathways of disease, thus addressing basic research and clinical questions [1], [2]. This technology, in the form of hybrid imaging modality combining PET with either CT or MRI, is widely deployed in clinical setting to aid in diagnosis, staging and restaging, monitoring of treatment response and radiation treatment planning of a wide range of oncologic malignancies [3], [4]. The bulk of research to date in PET instrumentation focused on development of high performance detector modules with the aim to achieve optimal image quality from high temporal resolution time-of-flight (TOF) technology, improving the sensitivity through increasing the axial coverage, and integration of solid-state photodetectors (e.g., SiPMs) on (digital) clinical PET scanners [5], [6], [7]. There is also growing interest in the development and deployment of dedicated small-bore intraoperative PET scanners for *ex vivo* surgical margins assessment in radioguided surgery [8], [9].

The literature is abundant of clinical studies unequivocally demonstrating that incorporation of TOF information in PET image reconstruction improves signal-to-noise ratio (SNR) and lesion detectability which can lead to reduction of acquisition time, thereby increasing patient comfort and scanner throughput [10], [11]. Yet, the magnitude of this improvement is correlated with patient size and coincidence time resolution (CTR). The CTR of the first modern commercial TOF-PET system, the Philips Gemini TF, was 585 ps [12], which was later reduced 310 ps following the introduction of digital technology [13], and more recently to ∼210 ps [14]. The quest for ultrahigh CTR TOF PET, toward the concept of reconstruction-free PET imaging [15], [16], remains an active research area with considerable potential [17], [18]. The improved timing resolution of the Biograph Vision.X compared to the Biograph Vision is expected to enhance TOF gain, thereby increasing the SNR [19].

The Biograph Vision PET/CT family features a unique gantry frame with detector electronic assembly (DEA) positioning rails, modular DEA design, DEA easy-grip handles, and accessible DEA cable connectors to enable unified in-field upgradability. The Biograph Vision.X (Siemens Healthineers, Knoxville, TN) builds on the design and hardware of the digital Biograph Vision 600 scanner but uses exclusive proprietary high-performance DEA technology and optimized digital electronics and digital processing along the entire imaging chain to achieve fast TOF performance. The DEA is installed within the shell of the gantry. Optimized digital electronics and digital processing are implemented along the entire imaging chain. The scanner features Siemens' Optiso ultra dynamic range (UDR) detector technology, which exploits numerous technologies to achieve optimal performance at different count rates.

Characterization of the performance of PET scanners is commonly carried out using the National Electrical Manufacturers Association (NEMA) standards [20]. This protocol was used to evaluate the performance of several commercial PET/CT and PET/MRI systems [13], [21], [22], [23], [24], [25], [26]. In particular, the performance characteristics of the Biograph Vision 600 PET/CT system were previously reported [14], [27]. The same system installed in our center in January 2019 exhibited almost similar performance characteristics to those reported in the reference above. This work aimed to evaluate the performance characteristics of the newly introduced Biograph Vision.X PET/CT system according to the NEMA NU 2-2018 standards [19]. In addition to the standard NEMA tests, we also report the energy resolution of the scanner and illustrations from the Hoffman 3-D phantom and clinical brain and whole-body PET studies. Although the differences between the Biograph Vision 600 and Vision.X scanners are not substantial for some parameters, the aim is to have self-standing publication serving as reference for the Vision.X PET/CT scanner for future clinical research studies.

II. Materials and Methods

A. Biograph Vision.X PET/CT System Specifications

The Biograph Vision.X shares similar physical specifications with its predecessor, the Biograph Vision 600 [14], featuring an 128-slice CT scanner and a whole-body PET scanner with 78 cm bore diameter (82 cm detector diameter) and a maximum patient weight capacity of 227 kg (total system weight: 3759 kg). The PET system consists of eight rings of lutetium oxyorthosilicate (LSO) detectors, with 38 detector blocks per ring. Each pair of adjacent detector blocks is operated by one electronics assembly unit, totaling 19 units per ring. Each detector block spans a 32-mm axial field-of-view (FOV) resulting in a combined 26.1 cm axial FOV across all 8 rings (including spacing between the blocks). The detector blocks are arranged in a 4×2 configuration, with 2 mini blocks axially, each containing a 5×5 matrix of LSO crystals, each crystal measuring $3.2 \times 3.2 \times 20$ mm. The mini blocks are coupled to a 16×16 mm silicon photomultiplier (SiPM) array, with 16 output channels per mini block for signal readout. The SiPM arrays fully cover the crystals, enhancing light collection which results in improved timing accuracy, and SNR. In addition, like its predecessor, the Vision 600, the Biograph Vision.X also benefits from small crystal sizes, contributing to improved spatial resolution, and uses the same energy window (435–585 keV) and coincidence time window (4.7 ns).

B. NEMA Performance Measurements

The performance evaluation covered spatial resolution, sensitivity, count rates [including true, random, scatter, and noise equivalent count rates (NECRs)], quantification accuracy, image quality, TOF resolution, and PET/CT coregistration. Each measurement adhered to the NEMA NU 2-2018 standards. The manufacturer supplied NEMA-compliant acquisition and reconstruction protocols. All reported performance parameters align with the specifications and definitions set forth by the NEMA NU 2-2018 standards [20].

Spatial Resolution: Considering the NEMA NU 2-2018 recommendations, a 370 kBq Na-22 point source (Eckert and Ziegler Isotope Products) at the time of the measurement, with a 0.250-mm diameter, was used for spatial resolution measurement. The activity was low enough to retain the dead-time and random losses below 5%. Using a resolution L-fixture and foam holders, the point source was located at various positions in the FOV with radial, tangential, and axial offsets of 1, 10, and 20 cm, respctively. For each position, the scan was acquired until 2 million true coincidences are recorded. The acquired sinogram data were reconstructed using 3-D Direct Inversion Fourier Transform for TOF (3D-DIFTOF) [28], a Fourier-based analytical reconstruction with a standard ramp filter, according to NEMA NU 2-2018. The images were generated as a $440 \times 440 \times 159$ matrix with a pixel size of 1.646 mm. Reconstructions were performed with normalization, deadtime, radial arc, decay, frame length and randoms correction but without corrections for attenuation or scatter. The spatial resolution was reported as the full-width at half-maximum (FWHM) and full-width at tenth maximum (FWTM) of the point-spread function (PSF).

Sensitivity: A 70 cm long polyethylene tube with inner and outer diameter of 1 and 3 mm, respectively, was filled carefully (avoiding air bubbles) with 4.49 MBq of ^{18}F and was placed inside the 5 concentric NEMA NU 2-2018 aluminum sleeves. Data was acquired 5 times, first with all the sleeves on and then removing one sleeve at a time until only the smallest sleeve is left. The whole measurement was conducted once at the center of the FOV and once with a 10 cm radial offset. System sensitivity was calculated based on the obtained data.

Count Rates (Trues, Randoms, Scatters, and Noise Equivalent Count Rates): The NEMA phantom, a 70 cm long 20 cm diameter polyethylene cylinder, was used for this measurement. A line source of 1294 MBq of ^{18}F was inserted into the axial pass-through hole in the phantom with a radial offset of 4.5 cm from the center. Data were acquired for a total of 11.4 h, in 35 frames each 240 s long and 1200 s between the frames. The NECR was calculated for two values of the factor K, which depends on how the randoms are estimated, namely $K = 0$ when randoms were calculated from detector singles rates or smoothed delayed sinogram data and $K = 1$ if the delayed sinogram were applied without smoothing or interpolation [29].

Accuracy (Correction for Count Losses and Randoms): The same data acquired for the previous measurement were used here. A low-dose CT scan was acquired to perform attenuation correction and model-based scatter correction. Following the corrections, the standard reconstruction algorithm provided by the manufacturer was used to reconstruct the images. This included an ordinary Poisson ordered-subset expectation maximization (OP-OSEM) 3-D iterative method to produce images in a 440×440 matrix. The applied corrections included, normalization, deadtime, attenuation and model-based scatter correction, and 2 mm (FWHM) Gaussian smoothing. Count-rate accuracy was assessed by extrapolating true rates at low activity levels, where count losses and random coincidences are minimal.

Image Quality and Accuracy of Corrections: For image quality assessment, the PET NEMA NU 2 image-quality phantom, equipped with six fillable spheres and a lung insert, was used. To achieve approximately one-fourth (1:4) activity concentration ratio between the background and the spheres, one quarter of the phantom tank was filled with a mixture of water and 50 MBq of ^{18}F. This mixture was then used to fill all the spheres. Thereafter, water was added to fill completely the phantom, and the lung-equivalent insert added. Given the total tank volume of 10 liters, the injected activity resulted in a background concentration of approximately 5 kBq/mL. The phantom was positioned on the scanner bed, with a scatter cylindrical phantom containing 111 MBq of ^{18}F placed axially beside it to simulate clinical scanning conditions.

After acquiring a topogram and aligning the center of the FOV with the spheres center, data acquisition was performed over 237 s, followed by a low-dose CT scan for attenuation correction. Corrections were applied for random coincidences (using smoothed randoms correction), normalization, decay, dead-time losses, scatter, and attenuation. The data were reconstructed using an OP-OSEM 3-D iterative algorithm with 8 iterations and 5 subsets resulting in $440 \times 440 \times 159$ matrix, with $1.65 \times 1.65 \times 1.65$ mm^3 voxel size. Three different images were generated and analyzed: 1) incorporating TOF and 2-mm Gaussian smoothing; 2) incorporating only TOF (no filtering); and 3) incorporating PSF and TOF (no smoothing). The assessments included percentage contrast for the spheres, background count variability for each sphere, and the lung residual error percentage. The recovery coefficients (RCs) were reported in terms of peak standardized uptake value (SUV_{peak}) calculated for a spheric region with a diameter of 10 mm centered on SUV_{max}.

TOF Coincidence Time and Energy Resolution: The same data used for the evaluation of the count rates was used to evaluate the TOF resolution. The later was calculated as the FWHM of the event time distribution, with corrections applied for scatter, random coincidences, and the line source position [20], [30]. The conventional technique involving the use of 19-cm-long ^{68}Ge line source with a diameter of approximately 2 mm having an activity of 10.3 MBq in air (without scattering medium) placed at the center of the FOV was employed. The energy resolution was calculated as the full width at half maximum of the measured energy spectrum.

PET/CT Coregistration Accuracy: For this test, an 1.3 ml vial was prepared containing a mixture of 37 MBq of ^{18}F (in the smallest volume possible) mixed with iodine contrast agent. A total load of 115 kg nominal weight, divided into increments of 11.5 kg plus the 11.5 kg L-fixture, was placed on the patient's bed. Source holders, provided by the manufacturer, were mounted on the L-fixture at six specific locations divided into two sets of three points located in each of two transaxial planes. In the transverse plane (with origin coordinates $x = 0$ and $y = 0$ cm), the holders were positioned at nominal coordinates of (0, 1 cm), (0, 20 cm), and (20, 0 cm) along the x and y axes. Along the axial plane (origin $z = 0$ at the edge of the PET axial FOV), holders were positioned at the center of the PET axial FOV ($z = 1/2$ PET axial FOV) and at 5 cm and 100 cm from the end of the patient table. At each location, a low-dose CT scan was acquired, followed by a 3-min PET scan. A total of six measurements were obtained to identify the centroids within both PET and CT datasets. Reconstruction was carried out using OP-OSEM algorithm (10 iterations, and 5 subsets) without post-reconstruction filtering. The produced images had image matrices of 440×440, and 512×512 for PET and CT, respectively. The 3-D vector length between the CT and PET centroids (coregistration error) was then calculated based on these centroid locations.

C. Hoffman 3-D Brain Phantom Study

The Hoffman 3-D brain phantom was scanned on both the Vision.X and Vision 600 scanners. The phantom was injected with 37.4 MBq and scanned 57 and 79 min post-injection on the Vision 600 and Vision.X, respectively. Both scans were acquired for 20 min and the images reconstructed using OP-OSEM (5 iterations and 5 subsets) considering PSF and TOF, and post-reconstruction 2-mm Gaussian smoothing into a matrix size of 440×440 with $0.825 \times 0.825 \times 1$ mm voxel size.

D. Clinical Studies

Representative patient studies are presented to offer a preliminary insight into clinical performance. However, a comprehensive and rigorous intersystem comparison is not the focus of this work. Our analysis focused on two patients scanned on the Biograph Vision.X and its predecessor the Vision 600 scanner. The study protocol is in accordance with the Declaration of Helsinki and was approved by the ethics committee of Geneva Canton (ID 2024-02232). Written informed consent was given by the subjects. The first patient is a 31-year-old male, weighting 92 kg, referred for a brain ^{18}F-FDG PET/CT scan. He was injected with 200 MBq and scanned for a duration of 10 min at 31 and 53 min post-injection on the Biograph Vision 600 and on the Biograph Vision.X, respectively. Both images were reconstructed using OP-OSEM (5 iterations and 5 subsets) considering PSF and TOF, followed by 2-mm Gaussian smoothing. They had a matrix size of 440×440 with $0.825 \times 0.825 \times 1$ mm voxel size.

TABLE I
RESULTS OF PET SPATIAL RESOLUTION MEASUREMENTS USING A ^{22}NA POINT SOURCE ON THE BIOGRAPH VISION.X COMPARED TO THE BIOGRAPH VISION 600 PET/CT SYSTEM

Spatial Resolution	Distance (cm)	Biograph Vision.X		Biograph Vision 600 [14]	
		FWHM (mm)	FWTM (mm)	FWHM (mm)	FWTM (mm)
Radial	1	3.4	6.8	3.5	6.8
	10	4.4	8.2	4.5	8.4
	20	5.7	10.2	5.8	11.1
Tangential	1	3.5	7.0	3.6	6.9
	10	3.5	7.0	3.9	7.0
	20	3.4	6.8	3.5	6.4
Axial	1	3.5	7.1	3.5	7.1
	10	3.7	7.4	4.3	8.7
	20	3.9	7.8	4.4	9.4

The second patient was a 61-year-old male (height of 175 cm and weighting 74.8 kg) who underwent a whole-body ^{18}F-FDG PET/CT scan. The patient was injected with 256 MBq and scanned using continuous bed motion with a speed of 0.7 mm/s (equivalent to 3 min per bed position), sequentially 82 and 110 min after injection on the Vision 600 and Vision.X, respectively. Both images were reconstructed using OP-OSEM (5 iterations and 5 subsets) considering TOF and PSF, and a 3-mm Gaussian filter using a matrix size of 440 $\times$ 440 with 1.65 $\times$ 1.65 $\times$ 1.4 mm voxel size. A total of 21 organs were segmented on whole-body PET images using previously developed deep learning models [31]. In addition, malignant lesions were segmented on PET images from both the Vision 600 and Vision.X scanners initially using a deep learning model and corrected manually by a nuclear medicine physician. The SUV_{mean} was compared between the two images and line profiles drawn on one lesion. Besides, the brain images were registered to the MNI Hammersmith atlas and the average uptake in 73 regions compared between brain images of the same patient scanned on both scanners.

III. RESULTS

A. Spatial Resolution

Table I summarizes the results of spatial resolution measured in three directions at distances of 1, 10, and 20 cm in terms of FWHM and FWTM along with a comparison with previously reported values for the Vision 600 scanner [14]. A trend of slightly improved axial resolution was observed in the Biograph Vision.X compared with Biograph Vision 600, especially when the point source was moved farther from the center. Plots of radial, tangential, and axial resolution results depicting both the FWHM and FWTM results for both scanners are also shown in supplemental Fig. 1 to allow for a much better comparison.

B. Count Rates: Trues, Randoms, Scatters, and Noise Equivalent Count Rates

Trues rate of 1230 kcps was achieved at 51.2 kBq/ml activity concentration compared to 1306 kcps at 54 kBq/ml

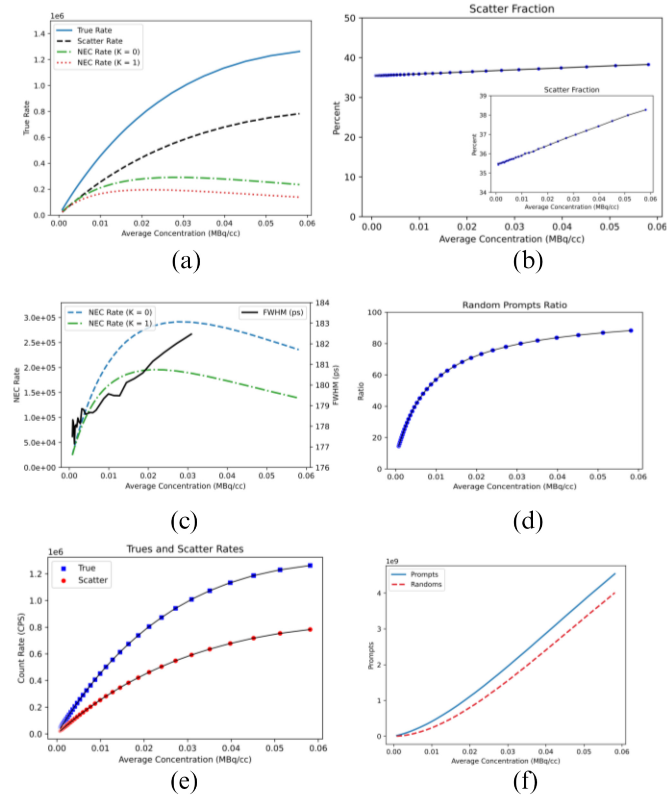

Fig. 1. Plots of count rate response, scatter, true, and random rates across different activity concentrations. (a) True and scatter count rate as well as NEC plots versus average activity concentration. (b) Scatter fraction variation with activity concentration where the small subfigure displays a zoom over the plot to better show the scatter fraction changes. (c) Plots of noise equivalent count rate versus activity concentration ($K = 0$ for noiseless estimate of random events and $K = 1$ for noisy random counts estimate as per NEMA standards) and TOF timing resolution. (d) Random prompts ratio changes with activity concentration. (e) True and scatter count rates relation. (f) Total prompt and randoms count rates versus activity concentration.

reported by van Sluis et al. [14] for the Vision 600 scanner. The peak NEC appears to be reached at lower than the usual value measured in factory (30 kBq/cc) (System specifications: Biograph Vision.X PET/CT, Siemens Healthineers). Table II summarizes the measured count rate performance and TOF time resolution on the Vision.X and compares them to the values reported for the Vision 600 scanner.

Fig. 1 depicts the trues and scatter rates as well as randoms to prompts ratio, the TOF resolution as well as the count rate performance and the NECR (for K=0 and K=1), and scatter fraction measured over different activity concentrations. The scatter fraction varies from 35.49% at the lowest activity concentration to 38.27% for the highest activity concentration.

C. Accuracy: Correction for Count Losses and Randoms

The true count rate at low activity level was extrapolated to determine the amount of deviation (percent error) from that at high activity level. Fig. 2 shows a plot of the minimum, average, and maximum relative count rate errors measured on a range of activity concentrations.

TABLE II
DIFFERENT PERFORMANCE METRICS INCLUDING COUNT RATE, NECR, SCATTER FRACTION AND TIMING RESOLUTION FOR THE VISION.X SCANNER COMPARED WITH THE VALUES REPORTED FOR THE VISION 600

		Biograph Vision.X	Biograph Vision 600 [14]
COUNT RATE			
	Trues rate [kcps] at effective activity concentration [kBq/cc]	1,230 at 51.2	1,306 at 54
	Peak NECR [kcps] at effective activity concentration [kBq/cc]	291 at 27.2	306 at 32.6
	Scatter fraction at peak NECR [%]	36.8	38.7
	Scatter fraction at low activity [%]	35.4	37.0
ACCURACY			
	Mean bias (%) at peak NECR	4.4	2.9
TOF RESOLUTION			
	FWHM [ps] at peak NECR	182.0	215
	FWHM [ps] at 5.3 kBq/cc	178.7	210

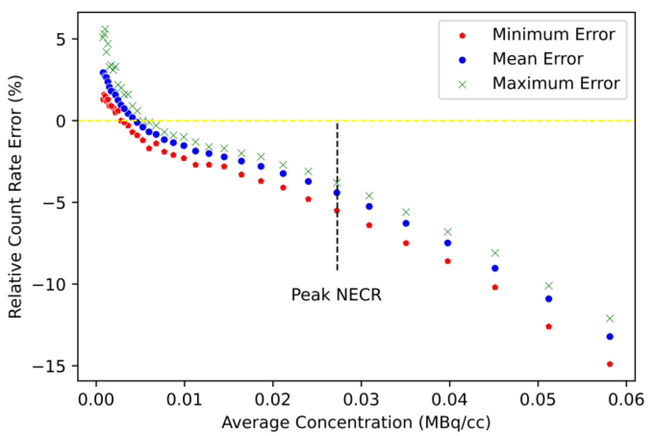

Fig. 2. Plots of the minimum, average, and maximum relative count rate error patterns as function of the activity concentration. The black vertical line depicts the peak NEC whereas the horizontal yellow line shows the zero-error line.

D. Sensitivity

A total sensitivity of 19.2 cps/kBq was observed at both 0 and 10 cm distances, resulting in the same value for the average. This value is also slightly high compared to factory measurements (16 cps/kBq) (System specifications: Biograph Vision.X PET/CT, Siemens Healthineers). Fig. 3 shows the axial sensitivity profile at 0 and 10 cm distances. The maximum sensitivity was observed at the center of the axial FOV as expected.

E. Image Quality and Accuracy of Corrections

A lung residual error of 0.9% was measured in the corresponding compartment of the NEMA image quality phantom. Table III summarizes the NEMA image quality metrics in terms of RCs, background noise, and variability for OP-OSEM iterative reconstruction with TOF and PSF. Overall, the image contrast observed on the NEMA image quality phantom ranged from 74.1% to 91.8% compared to 77.2% to 89.8% on the Vision 600 [14]. Fig. 4 shows the RC curves for three iterative different reconstruction algorithms measured in the NEMA image quality phantom with TOF and resolution recovery reconstructions.

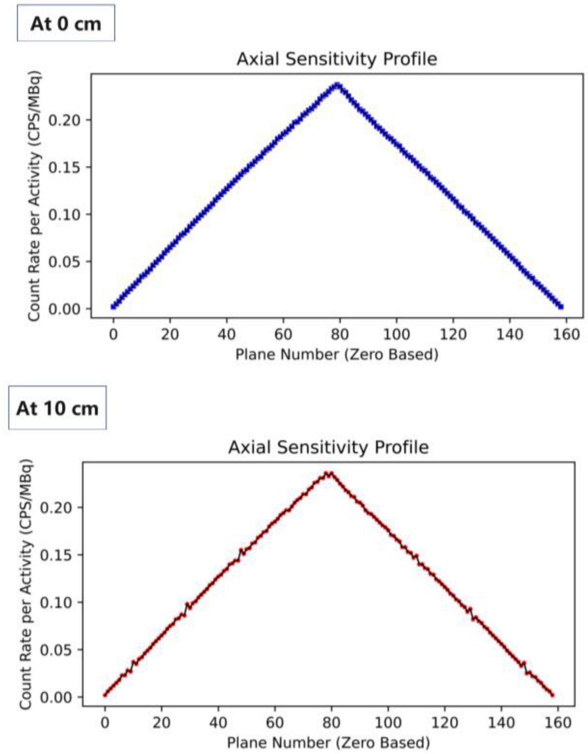

Fig. 3. Axial sensitivity profiles at 0 cm (top) and 10 cm (bottom) distances.

TABLE III
IMAGE QUALITY METRICS CALCULATED ON THE NEMA IMAGE QUALITY PHANTOM SHOWING RCs FOR SIX SPHERES AND THE BACKGROUND VARIABILITY FOR TOF-PSF RECONSTRUCTIONS WITH EIGHT ITERATIONS AND FIVE SUBSETS

Sphere size (mm)	10	13	17	22	28	37
Contrast (%)	74.1	72.2	80.3	82.4	91.1	91.8
Background variability (%)	7.3	5.9	4.5	3.4	2.3	1.8
Average lung residual error (%)	0.9					

F. TOF Coincidence Time Resolution, Energy Resolution, and PET/CT Coregistration Accuracy

TOF resolution of 178.7 ps at 5.3 kBq/cc degraded to 182.0 ps at peak NEC (3.32 ps or 1.85%). Peak NECR of 291 kBq/cc was observed at 27.2 kBq/mL activity concentration. The energy resolution measured using the ^{68}Ge line source was 8.3% at 511 keV, which was almost identical to the values reported for the Vision 600 (9%) [27] and Biograph Quadra (8.9%) [23] PET scanners. A maximum co-registration error of 1.74 mm was measured at 5 and 100 cm. Maximum ratio $R_{\max}$ of 0.09 and 0.15 mm was measured for CT and PET, respectively. It is worth emphasizing that PET/CT registration accuracy test, is not a measurement of a new system's performance but rather a test to demonstrate that the system was installed and aligned properly.

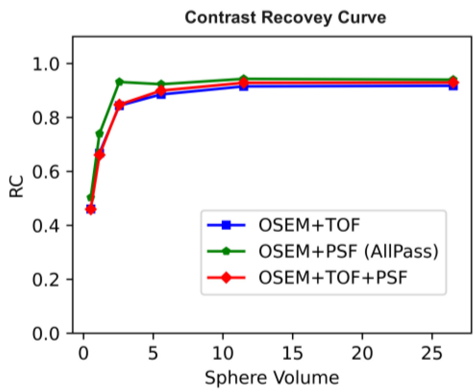

Fig. 4. RCs for different iterative reconstruction algorithms shown in the image measured using SUV_{peak}. Red diamond: OSEM using eight iterations and five subsets with TOF enabled reconstruction with resolution recovery and 2-mm Gaussian filter post processing. Green pentagon: OSEM using eight iteration and five subsets with resolution recovery only and no TOF and no post-reconstruction filtering, Blue cubic: OSEM using eight iterations and five subsets with only TOF enabled and 2-mm Gaussian filtering.

G. Hoffman 3-D Brain Phantom and Clinical Studies

Fig. 5 compares a representative slice of the Hoffman 3-D brain phantom and a clinical brain image scanned on both Vision 600 and Vision.X PET scanners. Nuclear medicine physicians reported a slight improvement in brain images acquired on the Vision.X compared to images acquired on Vision 600 scanner in terms of sharpness and overall contrast, especially in the basal ganglia and insula regions. This improvement can be noticed on the line profiles drawn on the transverse slices for the brain phantom and clinical images, as quantified by peak to valley ratio, though the second scan was performed on the Vision.X with slightly reduced randoms rate and there is greater washout of nonspecific tracer. It should be noted that the Vision 600 images were registered to Vision.X images through rigid-body registration for comparison.

Fig. 6 shows axial, coronal and maximum intensity projection (MIP) images of a whole-body ^{18}F-FDG clinical study where the patient was scanned sequentially on both scanners with 20 min time difference. Two different iterative reconstruction algorithms, including OP-OSEM with and without TOF and resolution recovery reconstruction were used. The patient presents with lung adenocarcinoma of the upper left lobe, treated with lobectomy and lymph node dissection 5 months prior to the PET scan. The images show multiple lymph nodes with increased tracer uptake compared to normal physiologic uptake. Nuclear medicine physicians reported slight improvement of image quality observed in the TOF images obtained on the Vision.X compared to the Vision 600 in terms of contrast and noise characteristics without noticeable difference in lesion detectability. The uptake time for the two scans may not be optimal to show real differences arising only due to scanner performance. Supplementary Figs. 2 and 3 show the region-wise comparison between brain PET images acquired on the Vision 600 and Vision.X scanners categorized by region of interest. Supplementary Fig. 4 shows the region-wise comparison of multiple lesions and organs segmented on whole-body PET/CT images from both scanners, while supplementary Fig. 5 depicts comparison of line profiles drawn on a malignant lesion.

IV. Discussion

The spatial resolution is not significantly improved in the Vision.X compared to its predecessor, the Vision 600. There is slight but no significant difference in axial spatial resolution measured using ^{22}Na point source between the Biograph Vision.X and previously published results from the Biograph Vision 600 [14], axial spatial resolutions and at 10 and 20 cm, where the improvement was 0.6 and 0.5 mm, respectively. This was expected given that the two scanners use the same detector modules and readout technology. The improvement in the axial resolution is due to the use of a different reconstruction algorithm between the early software version of Vision 600 and the current software of Vision and Vision.X where FORE+FBP has been replaced by 3D-DIFTOF (direct inversion Fourier transform for TOF), a more accurate analytical reconstruction, of the same class of Fourier-based analytical reconstruction [28]. One advantage is that it produces improved axial resolution (lower FWHM) than Fourier rebinning (FORE) + filtered backprojection (FBP) used in [14].

The NEMA peak NECR was 291 kcps at 27.2 kBq/mL, which is almost similar to the one achieved by the Vision 600 but at lower activity concentration (32.6 kBq/mL for the Vision 600). The improved TOF resolution (178.7 ps) for the Vision.X is expected to render more effective noise reduction or better contrast enhancement compared with the Vision 600. The slightly higher sensitivity of the Vision.X (19.2 cps/kBq compared to 16.4 and 16.3 cps/kBq for the Vision 600 at the center and 10 cm radial off-set, respectively) was not expected and the reason is not clear to us, although all scanners can be slightly different in terms of performance characteristics [32].

The peak NECR measured on the Vision.X was comparable to the Vision 600 (291 versus 308 kpcs) but was achieved as lower activity concentration (27.2 versus 32.6 kBq/mL). The same can be said about the true count rate, which peaked at 51.2 and 54 kBq/mL activity concentrations on both scanners, respectively. This might be only an experimental variation and, as such, it would be interesting to compare this to other systems installed recently. The TOF timing resolution was 178.7 ps on the Vision.X compared to 210 ps on the Vision 600 and worsens only by 3.32 ps from low count-rate to peak NECR, reflecting stable over the clinically relevant count rate range. The TOF gain is commonly defined as the effective gain in sensitivity at the center of a 20 cm diameter uniform cylinder specified by the relation $D/\Delta x$ [33], where $\Delta x = c \cdot \Delta t/2$, c being the speed of light and Δt the CTR. Hence, the TOF gain improves from 6.2 for the Biograph Vision 600 to 7.5 for the Biograph Vision.X. It is well established that a high TOF time resolution operates as extra equivalent-counts amplifier and makes the scanner more immune to imperfections in data corrections [34]. Hence, a better TOF time resolution results in reduced image noise at an equivalent number of counts. This is a relevant advantage in whole-body imaging, particularly for high BMI patients. This

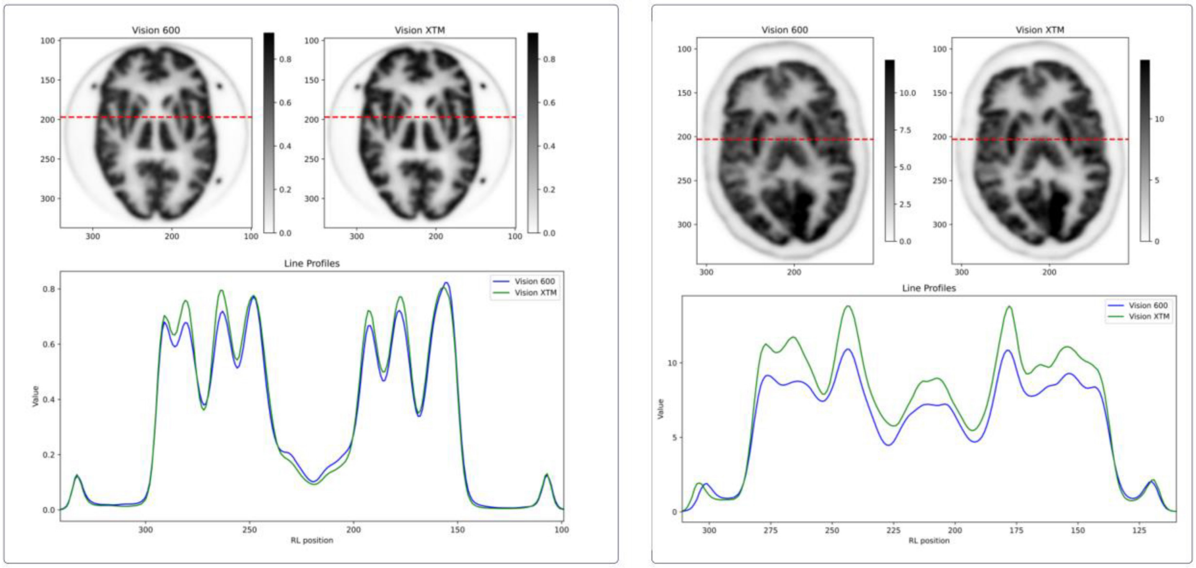

(a) (b)

Fig. 5. (a) Representative transverse slices of the Hoffman 3-D brain phantom with TOF and resolution recovery reconstruction. (b) Representative transverse slices of a clinical brain study scanned on both scanners. Horizontal line profiles through the images are also shown. The images were reconstructed using the identical reconstruction parameters (OSEM considering TOF, PSF using five iterations and five subsets, and 2-mm Gaussian smoothing). The color bar shows the SUV scales used for the display.

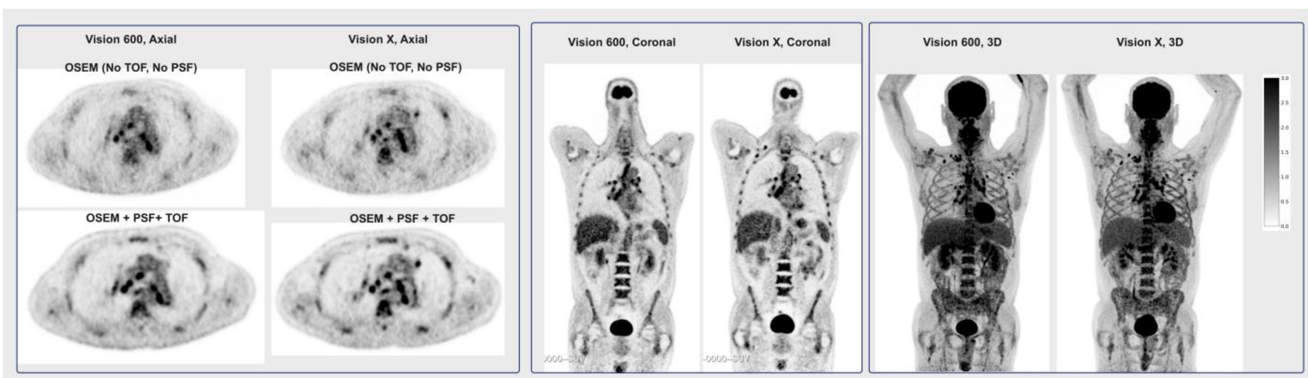

Fig. 6. Whole body ^{18}F-FDG clinical PET images of the same patient scanned both on the Vision.X and Vision 600 images. The images shown include transaxial slices on the left panel obtained using OSEM reconstruction algorithm, without and with TOF and resolution recovery reconstruction. The coronal and MIP images on the right panel depict images reconstructed using OSEM with TOF and resolution recovery on both scanners.

advantage is not fully exploited in the sense that the number of TOF bins used for image reconstruction is similar to the Vision 600 scanner. The enhanced TOF time resolution allows for improved SNR, particularly when taking full advantage of this improvement through listmode reconstruction [35]. This is being comprehensively evaluated using clinical studies focusing mostly on high BMI patients and the outcome will be reported in future studies.

The Vision.X exhibited high RCs for the small spheres of the NEMA image quality phantom. Similar to observations made in previous studies on the Vision 600 [14] and Vision Quadra [23], the contrast of the smallest sphere was artificially boosted owing to Gibbs artifacts typically encountered in resolution-recovery PET reconstructions [36]. In this study, we did not scan the same prepared phantom sequentially on both the Vision 600 and Vision.X scanners. Instead, we used values reported by Van Sluis et al. [14]. This may account for small variations arising from differences in phantom preparation between the two studies. The Hoffman 3-D brain phantom and clinical studies appear to suggest that the improved scanner performance might translate into superior delineation of smaller structures on high resolution brain PET images and improved contrast on the whole-body acquisitions.

One limitation of these sort of studies are that they only provide the performance of one particular PET scanner (N = 1); an average of several scanners installed at different locations would be more useful (N>2). To the best of our knowledge, this was done only once in very particular conditions and would be difficult to conduct [32].

V. Conclusion

The performance of a fast CTR clinical whole-body TOF PET/CT scanner was characterized. The Biograph Vision.X has better TOF timing resolution, which improved to 178.7 ps from 210 ps in the Vision 600, thus achieving 7.5 TOF gain improvement compared to 6.2 on the Vision 600. Overall, the initial clinical assessment reported no substantial difference between the two scanners.

Competing Interests

Habib Zaidi received funding from General Electric Healthcare not related to the present manuscript. Valentina Garibotto received research funding from Siemens Healthineers, GE Healthcare and Novartis and speaker fees from Siemens Healthineers, GE Healthcare, Novartis, BE imaging, Janssen and Bayer. The other authors have nothing to declare. The other authors declare that they have no known conflicts of interest in terms of competing financial interests or personal relationships that could have an influence or are relevant to the work reported in this article.

References

[1] T. Jones and D. Townsend, "History and future technical innovation in positron emission tomography," *J. Med. Imag.*, vol. 4, no. 1, 2017, Art. no. 11013, doi: 10.1117/1.JMI.4.1.011013.

[2] J. Schwenck et al., "Advances in PET imaging of cancer," *Nat. Rev. Cancer*, vol. 23, no. 7, pp. 474–490, Jul. 2023, doi: 10.1038/s41568-023-00576-4.

[3] J. Czernin, M. Allen-Auerbach, and H. R. Schelbert, "Improvements in cancer staging with PET/CT: Literature-based evidence as of September 2006," *J. Nucl. Med.*, vol. 48, no. 1S, pp. 78–88, 2007.

[4] C. Spick, K. Herrmann, and J. Czernin, "18F-FDG PET/CT and PET/MRI perform equally well in cancer: Evidence from studies on more than 2,300 patients," *J. Nucl. Med.*, vol. 57, no. 3, pp. 420–430, Mar. 2016, doi: 10.2967/jnumed.115.158808.

[5] N. Aide et al., "New PET technologies—Embracing progress and pushing the limits," *Eur. J. Nucl. Med. Mol. Imag.*, vol. 48, no. 9, pp. 2711–2726, Aug. 2021, doi: 10.1007/s00259-021-05390-4.

[6] J. M. M. Rogasch et al., "Moving the goalposts while scoring-the dilemma posed by new PET technologies," *Eur. J. Nucl. Med. Mol. Imag.*, vol. 48, no. 9, pp. 2696–2710, Aug. 2021, doi: 10.1007/s00259-021-05403-2.

[7] A. Sanaat, M. Amini, H. Arabi, and H. Zaidi, "The quest for multifunctional and dedicated PET instrumentation with irregular geometries," (in eng), *Ann. Nucl. Med.*, vol. 38, no. 1, pp. 31–70, Nov. 2024, doi: 10.1007/s12149-023-01881-6.

[8] H. Arabi, A. S. Manesh, and H. Zaidi, "Innovations in dedicated PET instrumentation: From the operating room to specimen imaging," *Phys. Med. Biol.*, vol. 69, no. 11, 2024, Art. no. 11TR03.

[9] A. Moraitis et al., "Evaluation of surgical margins with intra-operative PSMA PET/CT and their prognostic value in radical prostatectomy," *J. Nucl. Med.*, vol. 66, no. 3, pp. 352–358, Mar. 2025, doi: 10.2967/jnumed.124.268719.

[10] M. Conti and B. Bendriem, "The new opportunities for high time resolution clinical TOF PET," *Clin. Transl. Imag.*, vol. 7, no. 2, pp. 139–147, Apr. 2019, doi: 10.1007/s40336-019-00316-5.

[11] S. Surti, "Update on time-of-flight PET imaging," *J. Nucl. Med.*, vol. 56, no. 1, pp. 98–105, Jan. 2015, doi: 10.2967/jnumed.114.145029.

[12] S. Surti, A. Kuhn, M. E. Werner, A. E. Perkins, J. Kolthammer, and J. S. Karp, "Performance of Philips Gemini TF PET/CT scanner with special consideration for its time-of-flight imaging capabilities," *J. Nucl. Med.*, vol. 48, no. 3, pp. 471–480, 2007.

[13] I. Rausch, A. Ruiz, I. Valverde-Pascual, J. Cal-Gonzalez, T. Beyer, and I. Carrio, "Performance evaluation of the Vereos PET/CT system according to the NEMA NU2-2012 standard," *J. Nucl. Med.*, vol. 60, no. 4, pp. 561–567, Apr. 2019, doi: 10.2967/jnumed.118.215541.

[14] J. van Sluis et al., "Performance characteristics of the digital biograph vision PET/CT system," *J. Nucl. Med.*, vol. 60, no. 7, pp. 1031–1036, Jul. 2019, doi: 10.2967/jnumed.118.215418.

[15] G. Schramm, "Reconstruction-free positron emission imaging: Fact or fiction?" *Front. Nucl. Med.*, vol. 2, Jul. 2022, Art. no. 936091, doi: 10.3389/fnume.2022.936091.

[16] S. I. Kwon et al., "Ultrafast timing enables reconstruction-free positron emission imaging," *Nat. Photon.*, vol. 15, no. 12, pp. 914–918, Dec. 2021, doi: 10.1038/s41566-021-00871-2.

[17] D. R. Schaart, S. Ziegler, and H. Zaidi, "Achieving 10 ps coincidence time resolution in TOF-PET is an impossible dream," *Med. Phys.*, vol. 47, no. 7, pp. 2721–2724, Jul. 2020, doi: 10.1002/mp.14122.

[18] P. Lecoq et al., "Roadmap toward the 10 ps time-of-flight PET challenge," *Phys. Med. Biol.*, vol. 65, no. 21, Oct. 2020, Art. no. 21RM01, doi: 10.1088/1361-6560/ab9500.

[19] H. Zaidi, Y. Salimi, M. Amini, G. Mathoux, I. Mainta, and V. Garibotto, "Performance evaluation of the biograph vision.X: A high time-of-flight coincidence time resolution PET/CT scanner," *J. Nucl. Med.*, vol. 66, no. S1, 2025, Art. no. 251754.

[20] *Performance Measurements of Positron Emission Tomographs*, NEMA Standard NU 2-2018, 2018.

[21] H. Zaidi et al., "Design and performance evaluation of a whole-body Ingenuity TF PET-MRI system," *Phys. Med. Biol.*, vol. 56, no. 10, pp. 3091–106, May 2011, doi: 10.1088/0031-9155/56/10/013.

[22] B. W. Jakoby, Y. Bercier, M. Conti, M. E. Casey, B. Bendriem, and D. W. Townsend, "Physical and clinical performance of the mCT time-of-flight PET/CT scanner," *Phys. Med. Biol.*, vol. 56, no. 8, pp. 2375–2389, Apr. 2011, doi: 10.1088/0031-9155/56/8/004.

[23] G. A. Prenosil et al., "Performance characteristics of the biograph vision quadra PET/CT system with a long axial field of view using the NEMA NU 2-2018 standard," *J. Nucl. Med.*, vol. 63, no. 3, pp. 476–484, Mar. 2022, doi: 10.2967/jnumed.121.261972.

[24] T. Pan et al., "Performance evaluation of the 5-Ring GE Discovery MI PET/CT system using the national electrical manufacturers association NU 2-2012 standard," *Med. Phys.*, vol. 46, no. 7, pp. 3025–3033, Jul. 2019, doi: 10.1002/mp.13576.

[25] B. A. Spencer et al., "Performance evaluation of the uEXPLORER total-body PET/CT scanner based on NEMA NU 2-2018 with additional tests to characterize PET scanners with a long axial field of view," *J. Nucl. Med.*, vol. 62, no. 6, pp. 861–870, Jun. 2021, doi: 10.2967/jnumed.120.250597.

[26] B. Zhang et al., "Performance evaluation of new PET/CT DigitMI 930," *IEEE Trans. Radiat. Plasma Med. Sci.*, vol. 9, no. 5, pp. 578–585, May 2025, doi: 10.1109/TRPMS.2025.3526659.

[27] J. S. Reddin et al., "Performance evaluation of the SiPM-based siemens biograph vision PET/CT system," in *Proc. IEEE Nucl. Sci. Symp. Med. Imag. Conf. (NSS/MIC)*, Nov. 2018, pp. 1–5, doi: 10.1109/NSSMIC.2018.8824710.

[28] V. Y. Panin and S. Matej, "Three-dimensional Fourier-based reprojection analytic reconstruction from histoprojections for high-resolution time-of-flight positron emission tomography scanners," *J. Med. Imag.*, vol. 7, no. 3, May 2020, Art. no. 32505, doi: 10.1117/1.Jmi.7.3.032505.

[29] C. C. Watson et al., "Optimizing injected dose in clinical PET by accurately modeling the counting-rate response functions specific to individual patient scans," *J. Nucl. Med.*, vol. 46, no. 11, pp. 1825–1834, Nov. 2005.

[30] G.-C. Wang et al., "PET timing performance measurement method using NEMA NEC phantom," *IEEE Trans. Nucl. Sci.*, vol. 63, no. 3, pp. 1335–1342, Jun. 2016, doi: 10.1109/tns.2016.2522766.

[31] Y. Salimi, Z. Mansouri, I. Shiri, I. Mainta, and H. Zaidi, "Deep learning-powered CT-less multi-tracer organ segmentation from PET images: A solution for unreliable CT segmentation in PET/CT imaging," *Clin. Nucl. Med.*, vol. 50, no. 4, pp. 289–300, Apr. 2025, doi: 10.1097/rlu.0000000000005685.

[32] F. Schoenahl, "Performance characterization and development of quantitative procedures for PET-CT scanners," Ph.D. dissertation, Radiol. Med. Inform., Univ. Geneva, Geneva, Switzerland, 2011. [Online]. Available: https://archive-ouverte.unige.ch/unige:16769

[33] J. S. Karp, S. Surti, M. E. Daube-Witherspoon, and G. Muehllehner, "Benefit of time-of-flight in PET: Experimental and clinical results," *J. Nucl. Med.*, vol. 49, no. 3, pp. 462–470, Mar. 2008, doi: 10.2967/jnumed.107.044834.

[34] A. Mehranian and H. Zaidi, "Impact of time-of-flight PET on quantification errors in MR imaging-based attenuation correction," *J. Nucl. Med.*, vol. 56, no. 4, pp. 635–641, Apr. 2015, doi: 10.2967/jnumed.114.148817.

[35] D. Bharkhada, V. Panin, M. Conti, M. E. Daube-Witherspoon, S. Matej, and J. S. Karp, "Listmode reconstruction for biograph vision PET/CT scanner," in *Proc. IEEE Nucl. Sci. Symp. Med. Imag. Conf. (NSS/MIC)*, Nov. 2019, pp. 1–6, doi: 10.1109/NSS/MIC42101.2019.9059953.

[36] A. Rahmim, J. Qi, and V. Sossi, "Resolution modeling in PET imaging: Theory, practice, benefits, and pitfalls," *Med. Phys.*, vol. 40, no. 6, Jun. 2013, Art. no. 64301, doi: 10.1118/1.4800806.